The FEBS Journal

FEBS PRESS science publishing by scientists

Biochemical and structural characterization of chlorite dismutase enzyme from *Pseudomonas aeruginosa*

Dimitrios V. Nokas[1], Eleni K. Panagiotopoulou[1], Antonios I. Kapogiannatos[1], Georgios E. Premetis[1], Nikolaos E. Labrou[1], Eleni K. Efthimiadou[2], Anastassios C. Papageorgiou[3] and Evangelia G. Chronopoulou[1]

1 Laboratory of Enzyme Technology, Department of Biotechnology, School of Applied Biology and Biotechnology, Agricultural University of Athens, Greece

2 Inorganic Chemistry Laboratory, Department of Chemistry, National and Kapodistrian University of Athens, Zografou, Greece

3 Turku Bioscience Centre, University of Turku and Åbo Akademi University, Finland

Keywords

chlorite degradation; chlorite dismutase; Cld structure; Cld thermostability; heme *b*-containing oxidoreductases

Correspondence

E. G. Chronopoulou, Laboratory of Enzyme Technology, Department of Biotechnology, School of Applied Biology and Biotechnology, Agricultural University of Athens, 75 Iera Odos Street, GR11855, Athens, Greece

Tel: +30 2105294311

E-mail: exronop@aua.gr

(Received 22 September 2024, revised 5 April 2025, accepted 20 May 2025)

doi:10.1111/febs.70151

Industrialization and urbanization have caused serious contamination of water bodies, and the removal of chemical contaminants has become a major challenge. Chlorite is a harmful anthropogenic compound with a serious environmental impact and has been detected in groundwater, drinking water, and soil. Enzymes are considered sustainable tools for bioremediation, with chlorite dismutase (Cld) being a notable example. This enzyme has unique properties owing to the rare dioxygen bond formation that it catalyzes. In the present study, we report the cloning, biochemical, and structural characterization of the dimeric Cld from *Pseudomonas aeruginosa* (*Pa*Cld). *Pa*Cld is a heme *b* oxidoreductase that can decompose chlorite (ClO_2^- or $OClO^-$) into harmless chloride (Cl^-) and dioxygen (O_2) with high turnover rates. The structure of *Pa*Cld was determined at atomic (0.99 Å) resolution using X-ray crystallography. Additionally, steady-state kinetics and stability studies provided valuable insights into the catalytic mechanism of dimeric Clds. Apart from chlorite bioremediation of water, Clds can also be used in biomedical and synthetic biology as well as in enzymatic cascades with O_2-utilizing enzymes.

Introduction

Industrialization and urbanization have caused serious contamination of water bodies, and the global water management situation is alarming. Urgent and innovative technologies are required for reassuring the appropriate treatment of raw, processed, and sewage water [1,2]. In the next few decades, access to high-quality water is expected to worsen, and water scarcity is expected to occur globally [2]. Water pollutants can impact ecosystems and public health. Chlorite is an anthropogenic disinfection byproduct of serious environmental concern since it has been detected at rising concentrations in groundwater, surface waters, and soils [3]. In addition, chlorite causes hematological effects and affects behavior, sperm, and thyroid function [4]. Chlorite has also been found to cause severe cell damage *in vitro* [5,6]. Harmful quantities of chloro-oxyanions can exist on the surface and in groundwater because of the large-scale chemical production, wide range of applications, and chemical stability of chlorine anions in water. In addition, the COVID-19 pandemic has led to the increased use of chlorine-based disinfectants [7], making water treatment an essential practice.

Abbreviations

5cHS, five coordinated high spin; 6cHS, six coordinated high spin; 6cLS, six coordinated low spin; Cld, chlorite dismutase; eDNA, environmental DNA; NOB, nitrite-oxidizing bacteria; PCRB, (per)chlorate bacteria.; Rz, Reinheitszahlen number.

Enzymes are considered to be sustainable tools for bioremediation, and intensive research has been conducted in this field. Chlorite dismutase (Cld, EC1.13.11.49) is an enzyme that can be used for water purification. Cld is a heme *b*-dependent enzyme that has been classified as a chlorite O_2-lyase. Cld decomposes chlorite (ClO_2^- or $OClO^-$) with high turnover rates into harmless chloride (Cl^-) and dioxygen (O_2), with chlorite being the sole source of dioxygen [8,9].

The Cld gene exhibits a broad distribution across genomes and metagenomes. It was once believed to be a unique gene found only in perchlorate- and chlorate-reducing bacteria (PCRBs) [10], such as *Azospira oryzae* (GR-1), *Ideonella dechloratans*, *Dechloromonas aromatica*, and *Pseudomonas chloritidismutans*. The majority of characterized PCRBs belong to different classes of Proteobacteria and are anaerobic or microaerophilic [11], using ClO_3^- and ClO_4^- as electron acceptors. Specifically, ClO_4^- is reduced to ClO_3^- and then to ClO_2^-. This reduction pathway is catalyzed by (per)chlorate reductase, and the terminal product is the toxic chlorite ClO_2^-, which is degraded by Cld [12,13]. The Cld gene helps microorganisms to respond to reactive chlorine species along with other genes such as methionine sulfoxide reductase gene [10]. For example, *P. aeruginosa* combats chlorite toxicity through the methionine sulfoxide reductase (Msr) system, which can partially repair the methionine oxidized residues that are produced during Cld activity and O_2 production [14].

Cld has also been found and characterized in non-PCRB archaea and nitrite-oxidizing bacteria (NOB), such as *Candidatus Nitrospira defluvii* and *Nitrobacter winogradskyi* [11,15,16]. Chlorite formation from oxidative chemistry might also explain the presence of Cld in the nitrite-oxidizing bacteria. A study of comparative genomics of Cld has provided data for a deeper understanding of fluxes of oxidized chlorine species in different environments, and Cld was found to be involved in different biological processes. Chlorite is produced in microorganisms with enzymes that can reduce perchlorate and chlorate (that can also deposit from atmosphere) through metabolism or co-metabolism, and Cld prevents the formation of hypochlorous acid that can cause cell damage, while it produces beneficial oxygen. It has been proposed that microorganisms might detoxify hypochlorous acid by its oxidation to chlorite, which probably justifies Cld's presence in non-PCRB [10].

Clds are structurally related to other ancient and functionally mysterious protein families, including dye-decolorizing peroxidases [17]. Cld structures differ in the oligomeric state and architecture of their subunits, as they are also characterized by differences in sequence length [18]. Specifically, Clds have been categorized into two clades: the Clds of clade 1 are homopentamers or homohexamers with 'long' subunits consisting of two ferredoxin-like folds, whereas the Clds of clade 2 are homodimers with 'short' subunits, which lack most of the N-terminal ferredoxin-like fold. Both clades have similar C-terminal heme-binding ferredoxin-like folds and common features in their active centers [8,18,19]. Their active site endows them with peculiar enzymatic properties [20].

Clds, apart from their highly effective application in chlorite bioremediation of water, can also be used for *in situ* oxygen production for biomedical and synthetic biology applications, and for studying O_2-utilizing enzymes [9,21]. However, the application of enzymes in bioremediation and water treatment on a large scale is limited because of the complex composition, high salt concentration, and pH values of contaminated media that affect protein stability, recovery, and recycling. Therefore, the conformational and thermal stability of Cld needs to be studied to ensure its effective application in bioremediation [3]. One of the strategies to accomplish these requirements is through metagenome-derived genes from environmental samples, such as soil. Microbes can adapt to harsh environments through alterations in cellular physiology or mechanisms, many of which are based on novel enzymatic pathways [22,23]. The sample selection for gene mining is based on the desired enzyme functionality that is explored.

In this study, the Cld gene of *Pseudomonas aeruginosa* was amplified from environmental DNA (eDNA), cloned, and expressed in *Escherichia coli*. Biochemical and structural investigations of a dimeric clade 2 chlorite dismutase (*Pa*Cld) were conducted.

Results and Discussion

Cloning, expression, and purification of the recombinant PaCld enzyme

Chlorite dismutase is associated with respiratory perchlorate reduction in several Proteobacteria [24] and Pseudomonas has been identified as an active chlorine-tolerant bacterium [25]. Cld has been found as a greater proportion of genes in freshwater and soil systems [10], and accordingly, we selected a soil sample as a rich source of Proteobacteria (40%) (data not shown) for the isolation of the chlorite dismutase gene from *Pseudomonas aeruginosa*. Specific primers were used, and the amplified Cld gene was sequenced. Analysis of the amplified sequence via Protein-BLAST

revealed 100% amino acid sequence identity with chlorite dismutase from *Gammaproteobacteria* (NCBI Reference Sequence: WP_026084028.1.1) and 99.47% with chlorite dismutase from *Pseudomonas aeruginosa* (GenBank: MDC3951710.1). A search of UniProtKB revealed that the gene isolated from the soil sample exhibited 100% identity with a gene from *Pseudomonas aeruginosa* strain PA7 (NCBI: txid381754). The isolated gene was designated as *Pa*Cld. Its DNA sequence encodes a protein of 187 amino acids with a predicted molecular mass of 21 256 Da.

The *Pa*Cld gene was cloned into the vector pETite to generate the expression plasmid pETite-*Pa*Cld, which was subsequently expressed in *E. coli* C41(DE3) cells. The recombinant expression was assessed in eight *E. coli* strains: Lemo21 (DE3), Rosetta (DE3), Rosetta (DE3) pLysS, pLysS, C41 (DE3), Tuner (DE3), BL21 (DE3), and Origami B (DE3). Cultures exhibiting significant cell growth were selected and assessed for enzyme activity (Fig. 1A). Ultimately, *E. coli* C41 (DE3) cells were chosen for the expression of the Cld gene. Previous investigations have demonstrated that the moderate expression level of T7 RNA polymerase in the C41(DE3) strain promotes more efficient folding of P450s, compared to the BL21(DE3) strain [26]. *Pa*Cld was produced as a soluble intracellular protein, and its purification was performed through metal affinity chromatography, exploiting the 6-His tag at the C-terminal. The enzyme purity was assessed by SDS/PAGE electrophoresis (Fig. 1B) and SEC chromatography, where *Pa*Cld was eluted as a single, distinct peak (Fig. 1C).

Heme analysis and UV–vis spectral characterization

The heme absorption spectrum of *Pa*Cld exhibited maxima at 412 nm (Soret) and α/β bands at 531 and 564 nm (Fig. 2A), which are characteristic of heme *b*-containing Clds [27]. The occupancy of the active site with heme is reflected by the Reinheitszahlen number (Rz-value or purity number, A_{412nm}/A_{280nm}), which was determined to be equal to 2.56. This value is in agreement with the typical Rz-value for functional recombinant holoenzyme Clds [24,27]. Cld-like proteins often show low typical Rz-values, probably because of the weaker or hindered binding of heme compared to that of Clds [27].

The heme analysis based on the absorption spectra of *Pa*Cld revealed a Soret peak at 412 nm, along with three relatively weaker absorbance peaks at 531 and 564 nm (α/β bands) and 622 nm (CT1 band) at neutral pH (Fig. 2A,B). At alkaline pH 8, the resulting spectrum exhibited a sharpened Soret peak with Q-bands around 539 and 562 nm indicative of the presence of predominant low-spin 6-coordinated species (6cLS) (Fig. 2B) [24,28]. In addition, the ratio A_{Soret}/A_{380} was estimated (Table 1), since it is a good indicator of the amount of 5cHS species [24]. At approximately pH 4, *Pa*Cld loses its heme, displaying an absorption spectrum characteristic of free heme. At pH 5.5, the presence of a Soret maximum at 406 nm, a broad Q-band envelope at 504 nm, and a charge transfer (CT) band at 653 nm are features that are consistent with a five-coordinate high-spin (5cHS) heme [29]. At pH 6.0,

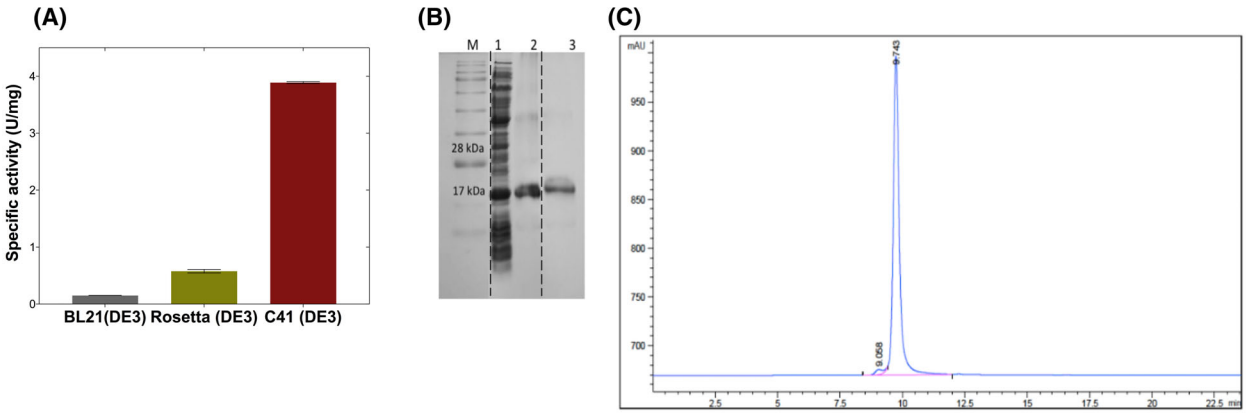

Fig. 1. Expression and purification study of *Pa*Cld. (A) Specific activity of *Pa*Cld expressed in different *E. coli* strains. All assays were performed in triplicate. The error bars represent the standard error. (B) SDS/PAGE analysis of the purification of *Pa*Cld by metal affinity chromatography (SDS/PAGE 12.5%w/v), (M) Pre-stained protein marker (Bluestar Prestained Protein Marker, Nippon Genetics Europe), (1) cell crude protein before purification, (2.3) best eluted fractions of purified enzymes that correspond to the band at ~22 kDa. Each sample contained 50 μg of total protein. The vertical dashed lines in the image indicate areas where the gel has been spliced together (C) Analytical size-exclusion chromatography (SEC) of the eluted fraction 3. Elution of *Pa*Cld was monitored by UV detection at 280 nm.

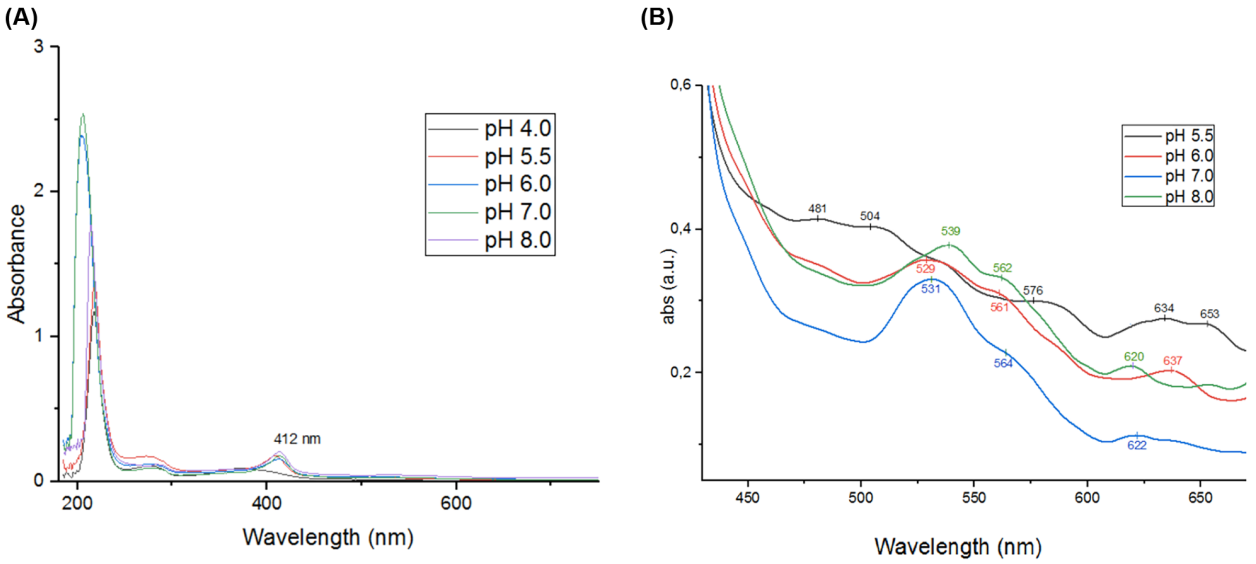

Fig. 2. UV–vis spectra of the variation of pH. (A) UV–vis spectra of *Pa*Cld at different pH values. All spectra were recorded at 25 °C. (B) Focus on visible bands on an expanded scale.

Table 1. Spectral parameters of recombinant wild-type chlorite dismutase *Pa*Cld at ferric state.

pH	Soret (nm)	α/β bands (nm)	CT bands (nm)	A_{Soret}/A_{380}	Predominant spin state species
5.5	406	576	504 634/653	1.93	5cHS
6.0	412	532/561	637	1.97	5cHS
7.0	412	531/564	622	2.60	6cLS
8.0	412	539/562	620	2.55	6cLS

a red-shifted Soret band can be seen that may indicate the presence of HS ferric heme six-coordinate (6c) complex (Fig. 2B). The HS species, predominant at acidic pH (5.5–6), was converted to LS species with increasing pH values as reported by the B band shifting to 412 nm and the charge transfer (CT) band losing intensity. These results demonstrate that the enzyme in acidic pH is most likely to stabilize an open coordination position at which an oxidant might catalyze. Band positions of the alkaline form are typical of low-spin hydroxide complexes of heme proteins with proximal His ligands [29]. *Pa*Cld has UV–visible features characteristic of a 6cLS species with a red-shifted Soret band at 412 nm and α/β bands at 531, 539, 564, and 562 nm, again suggesting the presence of ferric hydroxide at neutral and alkaline pH [24]. The dimeric *Nw*Cld and *Da*Cld variant W155F exhibit Soret maxima at 405 and 413 nm, respectively. The recombinant *Nw*Cld depicted spectral maxima at 506, 543, and 640 nm at neutral pH, which are indicative of predominant five-coordinate high-spin heme *b*. The *Da*Cld variant W155F charge transfer band (CT) at 660 nm and α/β bands at 535 and 565 nm at alkaline pH [24,27,28].

The pH dependence of enzyme activity and stability

The pH profile and optimal pH for the enzyme's activity were determined by assaying the enzyme at 30 °C over a pH range of 4.0 to 8.0. The dependence of enzyme activity on pH exhibited a bell-shaped profile. Optimal activity for *Pa*Cld was measured at pH 6.0 (Fig. 3A). Below pH 5.0 and above pH 7.0, the catalytic activity was diminished.

The enzyme showed operational stability at different pH values (Fig. 3B); however, its activity decreased dramatically below pH 5.0 (Fig. 3A).

Steady-state kinetics of chlorite decomposition and pH dependence of kinetic parameters

Wild-type *Pa*Cld was purified by metal affinity chromatography and subjected to dialysis before steady-state kinetic analysis. The chlorite-degrading activity and its pH dependence were measured by continuously monitoring O_2 production from chlorite decomposition using a Clark electrode (initial generation of μM O_2 per second at 30 °C). The reported K_M values for chlorite dismutases at pH 7.0 vary from 69

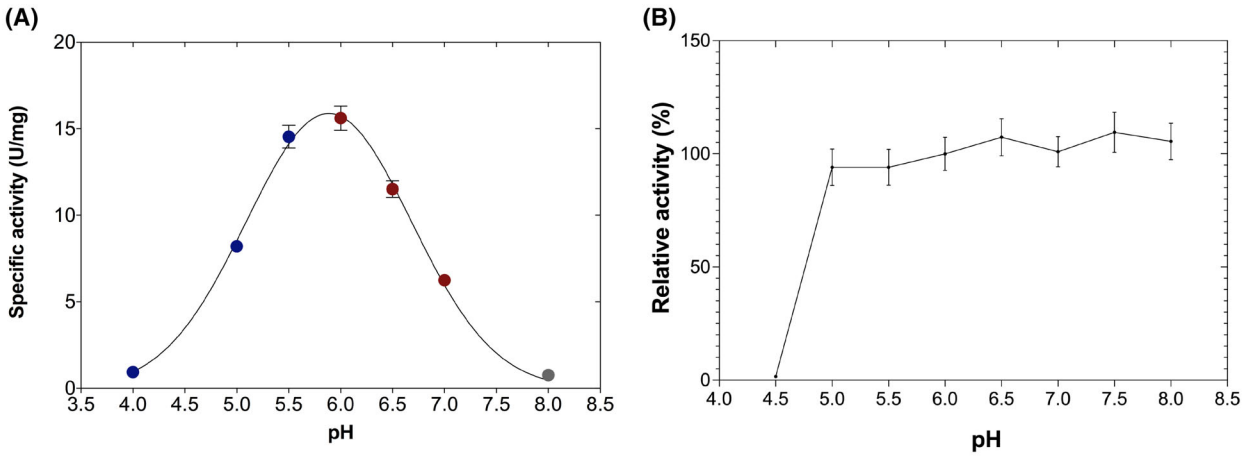

Fig. 3. Study of pH impact on *Pa*Cld. (A) Effect of pH on specific activity for *Pa*Cld. Enzyme activity was measured in the standard assay reaction at 30 °C, at pH values ranging from 4 to 9, and using the appropriate buffers. Blue, red, and gray color dots represent sodium acetate, potassium phosphate, and trizma base reaction buffer, respectively. (B) Enzyme stability at different pH values for 2 h at 25 °C, expressed as relative activity (%). The enzyme was incubated in the appropriate buffer and then added to the reaction solution at pH 6.0. Each pH incubation was assessed in at least three independent trials. The activity at pH 6.0 was taken as 100%. Values presented are given as a mean of three replicates ($n = 3$) ± SE.

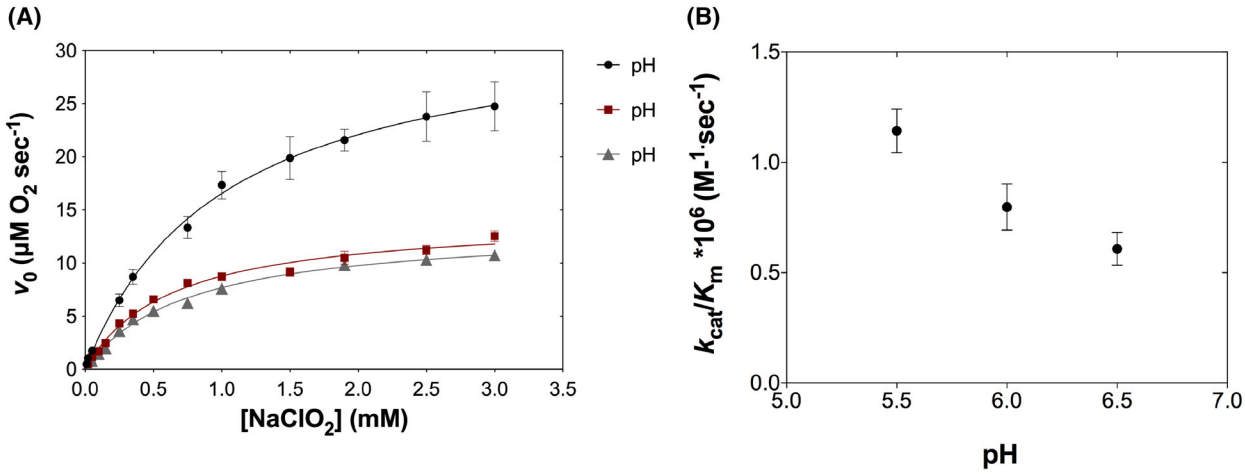

Fig. 4. Plot of the initial rate (v_0) of molecular oxygen release as a function of chlorite concentration at pH 5.5–6.5. (A) Michaelis–Menten plot at pH 5.5, 6.0, and 6.5; (B) pH dependence of catalytic efficiency (k_{cat}/K_M). Experiments were performed in triplicate. Values presented are given as a mean of three replicates ($n = 3$) ± SE. The enzyme concentration was 0.029 µµ.

to 260 µM, k_{cat} values from 43 to 7500 s^{-1}, and k_{cat}/K_M values from 6.2×10^5 to 3.5×10^7 $M^{-1} \cdot s^{-1}$ [27]. *Pa*Cld followed Michaelis–Menten kinetics for $NaClO_2$ (Fig. 4A). The pH dependence (pH 5.5, 6.0, and 6.5) of the kinetic parameters is shown in Table 2. There is a difference between K_M and k_{cat} with respect to the pH. Even though the K_M value was lower at pH 6.0, which showed the best affinity,

Table 2. Steady-state kinetic parameters of *Pa*Cld for $NaClO_2$. Influence of pH on K_M values, turnover number (k_{cat}), and catalytic efficiency (k_{cat}/K_M).

pH/°C	K_M (mM)	k_{cat} (s^{-1})	k_{cat}/K_M ($M^{-1} \cdot s^{-1}$)
pH 5.5/30 °C	1.01 ± 0.06	1145.0 ± 28.4	$1.14 \times 10^6 \pm 0.01$
pH 6.0/30 °C	0.62 ± 0.06	490.4 ± 16.8	$0.79 \times 10^6 \pm 0.10$
pH 6.5/30 °C	0.74 ± 0.06	446.5 ± 16.2	$0.61 \times 10^6 \pm 0.07$

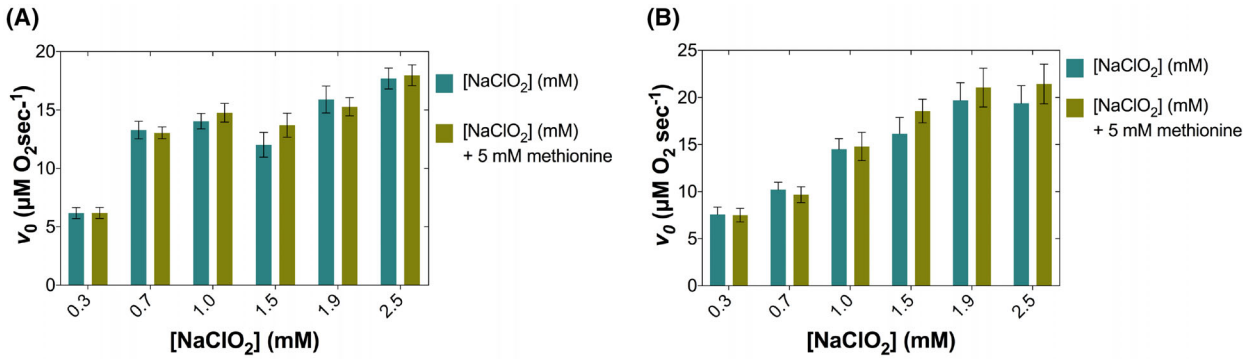

Fig. 5. Hypochlorite effect in *Pa*Cld inhibition. Effect of methionine on chlorite degradation and initial rate v_0 of O_2 released (µµ·s^{-1}) catalyzed by *Pa*Cld at pH 5.5 (A) and pH 6.0 (B). The enzyme concentration was 0.029 µµ. Each point corresponds to mean initial velocity determined by three replicates ($n = 3$). The error bars represent the standard error. Student's paired *t*-test was performed with GRAPHPAD PRISM. No significant statistical difference was found (*P*-values 0.40 and 0.12 at pH 5.5 and 6, respectively).

the k_{cat} value was better at pH 5.5. The catalytic efficiency k_{cat}/K_M showed pH dependence (Fig. 4B) with an optimum pH of 5.5 ($1.14 \times 10^6 \pm 0.01$ M^{-1}·s^{-1}). Upon increasing the pH, the O_2 yield decreased significantly.

*Pa*Cld belongs to the same cluster 'lineage II' as *Nw*Cld. *Nw*Cld is considered an efficient enzyme with pH optima of the chlorite-degrading activity at 5.5 and k_{cat}/K_M value of 2.1×10^6 M^{-1}·s^{-1} [11]. However, recombinant *Cyanothece sp*. PCC7425 (CCld) shows greater catalytic efficiency with a k_{cat}/K_M value of 7.1×10^6 M^{-1}·s^{-1} at an optimum pH of 5.0 [15]. Hypochlorite is formed during catalysis and has been found to be involved in irreversible inactivation of the enzyme [30]. To test whether hypochlorite is involved in *Pa*Cld inhibition and may play a role in catalytic efficiency at different pH levels, initial rate measurements were performed in the presence of 5 mM methionine. Methionine reacts with HOCl efficiently and quickly, without reacting with chlorite [31]. Assays were conducted at pH values of 5.5 and 6.0 in the presence of 5 mM methionine using the same enzyme concentration as in the enzyme kinetics. The effect of methionine on chlorite degradation by *Pa*Cld at pH values of 5.5 and 6.0 is depicted in Fig. 5. At low chlorite concentrations (0.3 and 0.7 mM), there is no effect of methionine, while in 1 mM concentration, the effect is small. However, at higher chlorite concentrations in the presence of methionine, the O_2 rate increased, and this effect was more pronounced at pH 6.0. Therefore, even if it seems that pH 6.0 is the optimum pH of the enzyme reaction, the turnover number (k_{cat}) and the catalytic efficiency (k_{cat}/K_M) showed the pH 5.5 as the optimum pH, probably because the inhibition reaction was boosted at pH 6.0.

Conformational stability evaluated by UV–vis spectroscopy

The stability of the heme cavity of *Pa*Cld was evaluated by chemical denaturation using guanidinium hydrochloride (GdnHCl). The release of the prosthetic group was monitored through Soret absorbance and was observed to follow a two-state transition (Fig. 6A, B). The conformational stability ($\Delta G°H_2O$) of *Pa*Cld was determined to be equal to 6.73 ± 0.52 kJ·mol^{-1} (Fig. 6C) depicting the midpoint of transition at 0.97 ± 0.03 M GdnHCl. The enzymes *Nd*Cld (homopentamer) and *Nw*Cld (dimer) depict conformational stability ($\Delta G°H_2O$) 12.7 ± 1.7 and 4.3 ± 0.8 kJ·mol^{-1}, respectively [3,16]. According to the midpoint of transition, *Pa*Cld seems to be less stable than *Nw*Cld.

Impact of temperature on enzyme activity and thermal stability of PaCld of holoenzyme

To assess the structural stability of the enzyme, thermal inactivation kinetics and UV–vis unfolding measurements were performed. The kinetics of thermal inactivation were measured in the range of 10–75 °C at two different pH values (6.0 and 7.0) (Fig. 7A). The thermal half-inactivation temperatures $T_{1/2}$ for pH 6.0 and pH 7.0 were found to be equal to 66.8 ± 0.5 and 68.8 ± 0.8 °C, respectively. Up to 55 °C at both pH values, *Pa*Cld retained nearly full enzymatic activity, while complete inactivation occurred at approximately 75 °C. The kinetics of thermal inactivation at 67 °C (Fig. 7B) follow first-order kinetics, indicating that the rate of inactivation is proportional to the amount of active enzyme remaining. The half-life $t_{1/2}$ ($t_{1/2} = 0.693/k_D$) at 67 °C was found to be 30.15 ± 0.78 min. The T_m based on the UV–vis

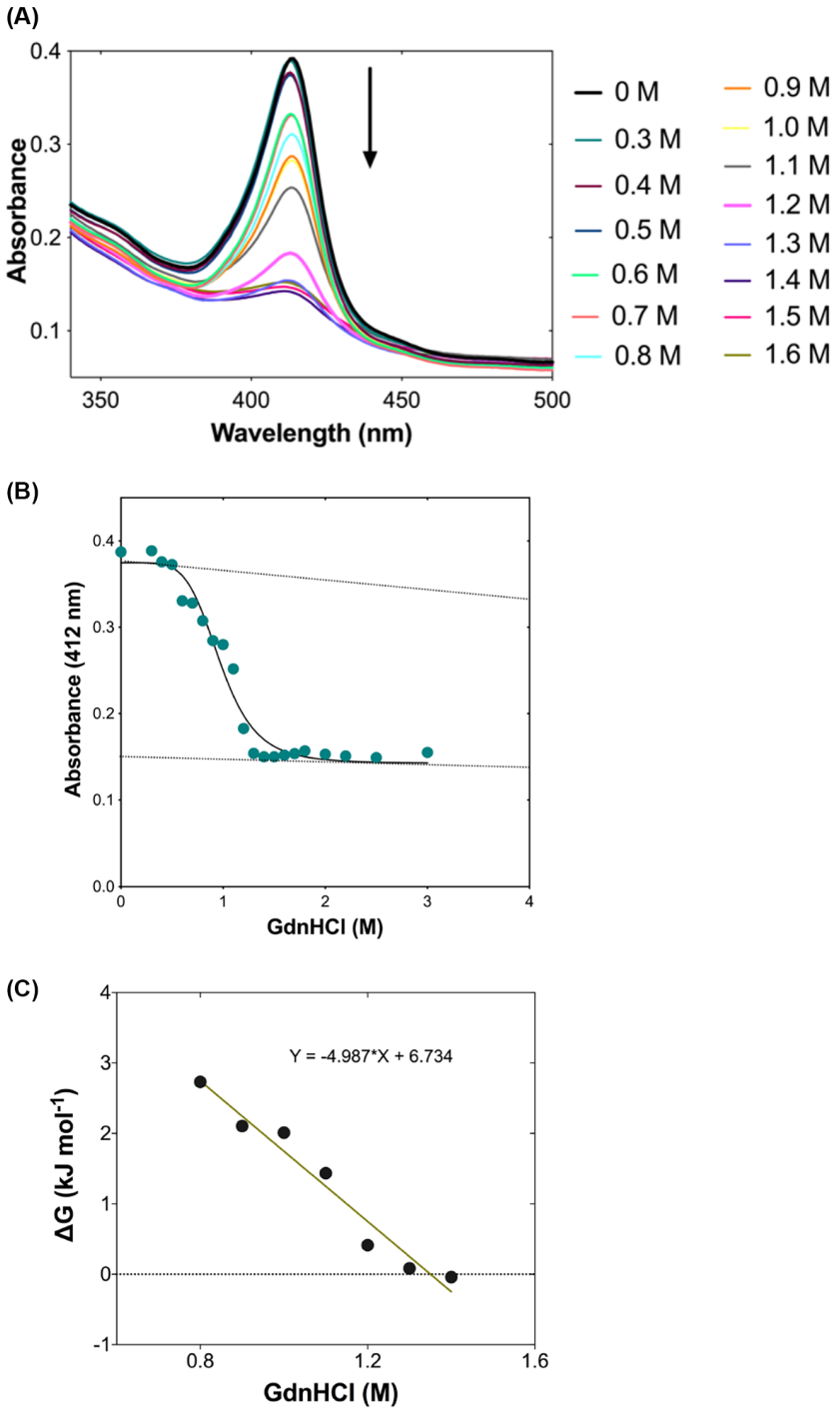

Fig. 6. Chemical denaturation of *Pa*Cld (2 μM) after its incubation with various concentrations of GdnHCl at room temperature. The denaturation was monitored by UV–vis spectroscopy. (A) Soret absorbance reduction (black arrow) upon increasing the concentration of guanidinium hydrochloride. (B) Plots of change in Soret maximum absorbance versus guanidinium hydrochloride concentration. (C) Plot of change in free energy at various GdnHCl concentrations.

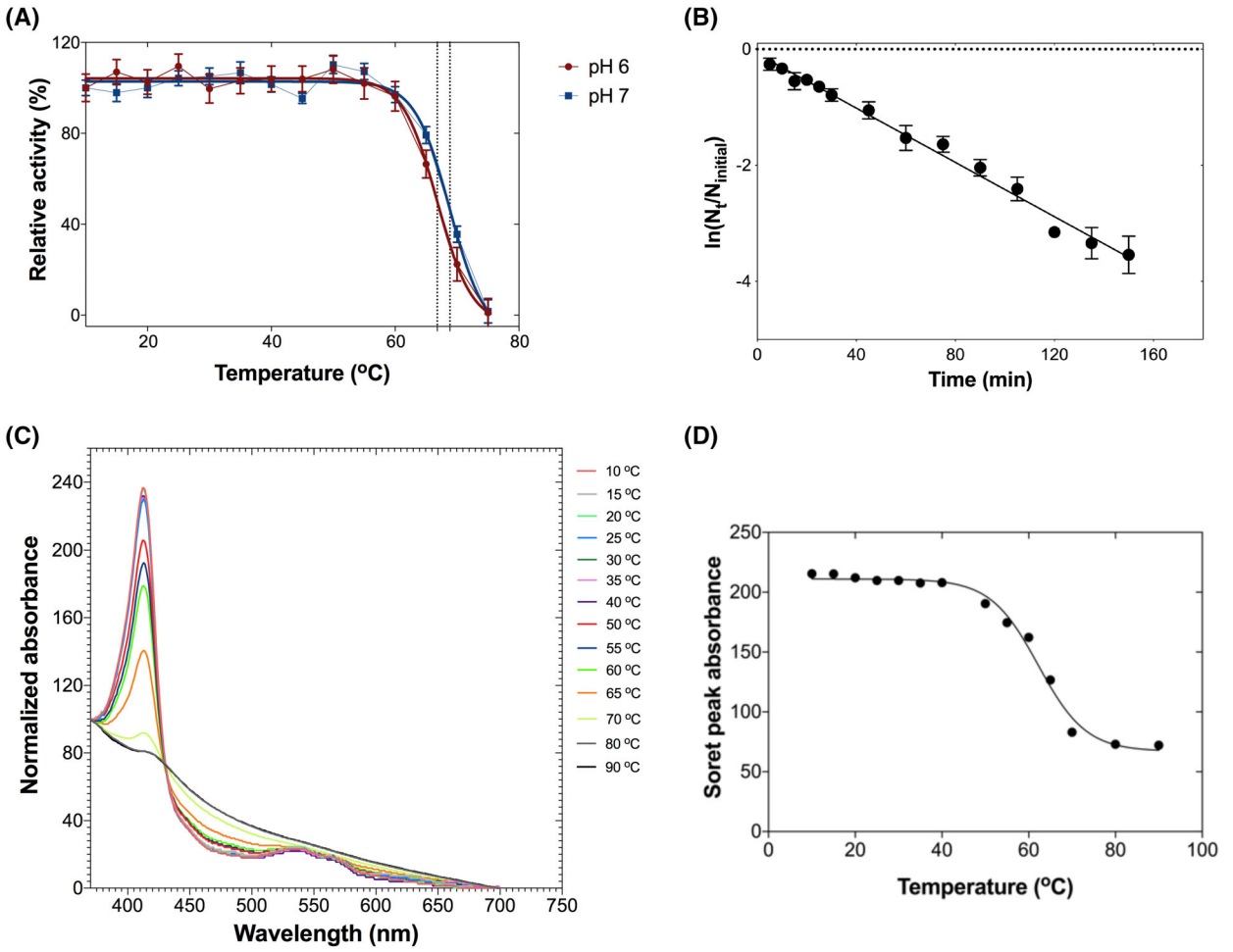

Fig. 7. Enzyme thermostability. (A) Enzyme residual activity curve for *Pa*Cld. The residual activities were measured after heat treatment at various temperatures (°C) for 5 min. Values presented are given as a mean of replicates ($n = 3$) ± SE. Dashed lines indicate the $T_{1/2}$ values. (B) Thermal inactivation kinetics at 67 °C. Each point corresponds to mean initial velocity determined by three replicates ($n = 3$). The error bars represent the standard error. (C) UV–vis spectral changes of *Pa*Cld under different temperatures. (D) Soret peak absorbance change under different temperatures.

spectroscopy was found to be equal to 62.2 ± 0.8 °C (Fig. 7C,D).

Crystallographic analysis and structural characterization of PaCld

The solved crystal structures of Clds have shown two distinct subunit topologies. The first topology ('long Clds') includes Clds from Lineage I and Cld-like representatives. The second subunit topology ('short Clds') includes functional Clds of Lineage II. Both topologies share a similar heme-binding C-terminal domain with ferredoxin-like fold [27]. Representatives of 'short Clds' are the Clds from *Nitrobacter winogradskyi* (PDB: 3QPI) and *Cyanothece sp.* (PDB: 5K90). The X-ray crystal structure of *Pa*Cld showed that *Pa*Cld also belongs to the second subunit topology. The sequence identity of *Pa*Cld with the dimeric Clds from *Nitrobacter winogradskyi* and *Cyanothece sp.* PCC7425 is 51.1% and 49.7%, respectively.

The structure of *Pa*Cld was determined at atomic (0.99 Å) resolution using X-ray crystallography. The enzyme was crystallized in a crystal form that displays the typical dimer found in other Clds [8,24]. The final structure (Table 3) exhibits good geometry as judged by several quality criteria. The electron density map for each subunit showed clear density of residues 1–186 (monomer A) and 3–186 (monomer B). All monomers contain one protoporphyrin IX (heme) and

Table 3. X-Ray data collection and refinement statistics.

Data collection	*Pa*Cld
Beamline	P13 (PETRA III, Hamburg)
Wavelength, (Å)	0.7749
Resolution (Å)	49.32–0.99 (1.02–0.99)
Space group	C2
Unit cell dimensions	
a, b, c (Å)	127.5, 46.0, 90.2
α, β, γ (°)	90, 129.3, 90
Unique reflections	217 930 (20 381)
Multiplicity	6.8 (7.0)
Completeness	97.2 (92.6)
Mean((I)/SD(I))	14.8 (0.8)
R_{meas}	0.049 (2.478)
$CC_{1/2}$	0.99 (0.36)
Wilson B-factor (Å^2)	14.0
Refinement	
Reflections (working/test)	215 885/1999
R_{cryst}/R_{free}	0.149/0.165
Rms deviation in bond lengths (Å)	0.009
Rms deviation in bond angles (°)	1.06
Number of protein/ligand/water atoms	3110/103/697
Average B-factor for all atoms/protein/ligand/water (Å^2)	18.8/16.4/12.6/30.0
Clashscore	3.40
Phi-psi plot, favored/outliers (%)	98.6/0.0
PDB id	9GTJ

Table 4. Summary of interface characteristics.

Parameter	*Pa*Cld (PDB: 9GTJ)	*Nw*Cld (PDB: 3QPI)	CCld (PDB: 5K90)
No. residues	31 (A), 31 (B)	25 (A), 25 (B)	25 (A), 27 (B)
Area buried at interface (Å^2)	1144	978	907
% of total surface	12.0	11.1	9.8
No. hydrogen bonds	18	18	12
No. salt bridges	12	10	10

one imidazole in the active site. The final model has good stereochemistry and R-factors and contains 2 heme molecules including 2 Fe^{3+}, 2 imidazole molecules, 6 sodium cations, 1 chloride anion, and 744 water molecules. The distal ligand of ferric Clds is typically a water molecule, but this ligand can be exchanged in the crystal structures with molecules of the crystallization liquid [27]. In the *Pa*Cld structure, imidazole has replaced the water molecule that coordinates the iron atom. The same has happened in the structure of *Nd*Cld; however, the water molecule Wat108 can be seen in the *Nw*Cld structure [11].

*Pa*Cld is a dimer with an interface similar to that of *Nw*Cld and CCld (Table 4) and entirely different from that observed in the pentameric or hexameric Clds [11]. Each subunit has one heme *b* and exhibits a ferredoxin-like fold that represents the most prominent common feature of all functional Cld [8]. *Pa*Cld subunit has an α + β structure consisting of an eight-stranded, antiparallel β-sheet forming a β-barrel, with the α-helices lying up to the β-sheet of the protein (Fig. 8A). Heme is bound in a well-defined pocket between the β-strands and α-helices of each *Pa*Cld monomer. *Pa*Cld, like *Nw*Cld, has longer loops between the β-strands at the interface. The dimer interface of *Pa*Cld is formed by residues from the loop between β4 and α1 that interacts with the loop between the helices α2' and α3' from the other monomer. There are two salt bridges in the interface characteristics for most Clds of lineage II; however, the interface of the pentameric *Nd*Cld has more hydrophobic character (about 30% hydrophobic) [11]. The pair residues involved in these salt bridges are Arg65-Glu104' and Arg61-Asp135' (Fig. 8B). Specifically, the first salt bridge is formed between Arg65, which is located in the loop between β4 and α1, and Glu104', which is found at the beginning of helix α3'. The main chain N atom of Arg61 interacts with the propionate group of heme *b* via hydrogen bonds (Fig. 8B, inset). This is a difference from the canonical (lineage I) Clds, which lack any obvious link between the subunit interface and heme binding [11].

The superposition of *Pa*Cld with the dimeric structures of *Nw*Cld and *Cyanothece sp*. PCC7425 showed that the loop of *Pa*Cld between β6 and β7 (residues 136–141 in *Pa*Cld) was longer than the loop of the other two structures (Fig. 8C). This loop may contribute to the stability of *Pa*Cld dimer through the hydrogen bonds formed between Glu138', Arg4, and Val5. Moreover, the loop between β3 and β4 is well defined in the atomic resolution structure of *Pa*Cld, suggesting that it may have less flexibility in *Pa*Cld. Although the residues of the β3-β4 loop do not contribute to dimer interface, their reduced flexibility may increase the stability of the *Pa*Cld molecule. Heme is also bound to the cavity through hydrogen bonding of amino acids Arg61, Tyr62, and Val63 to propionate at position 7 via their backbone nitrogen. *Pa*Cld, a typical clade 2 chlorite dismutase, has a distal Arg128 and a characteristic axial (Fe coordinating) residue His115, whose role is the coordination of heme iron [19]. The reaction occurs at a His-ligated 5-coordinate high-spin heme; however, the reaction details are not fully known and more data are needed for the actual molecular mechanism of catalysis [18,32]. The distance of proximal

histidine Nε2 to the iron atom is 2.03 Å. The flexible Arg128 is in the 'out' conformation as it is expected [33] and it is H-bonded with Gln75 (Fig. 8D). This conformation of Arg128 can support the chlorite cleavage and the placement of transient intermediates, while it seems to act as a gatekeeper for the active site [33].

The residues Lys93, Trp97, and His115 in the active site of *Pa*Cld are strictly conserved in all Clds and Cld-like proteins, while the five residues Ile89, Trp98,

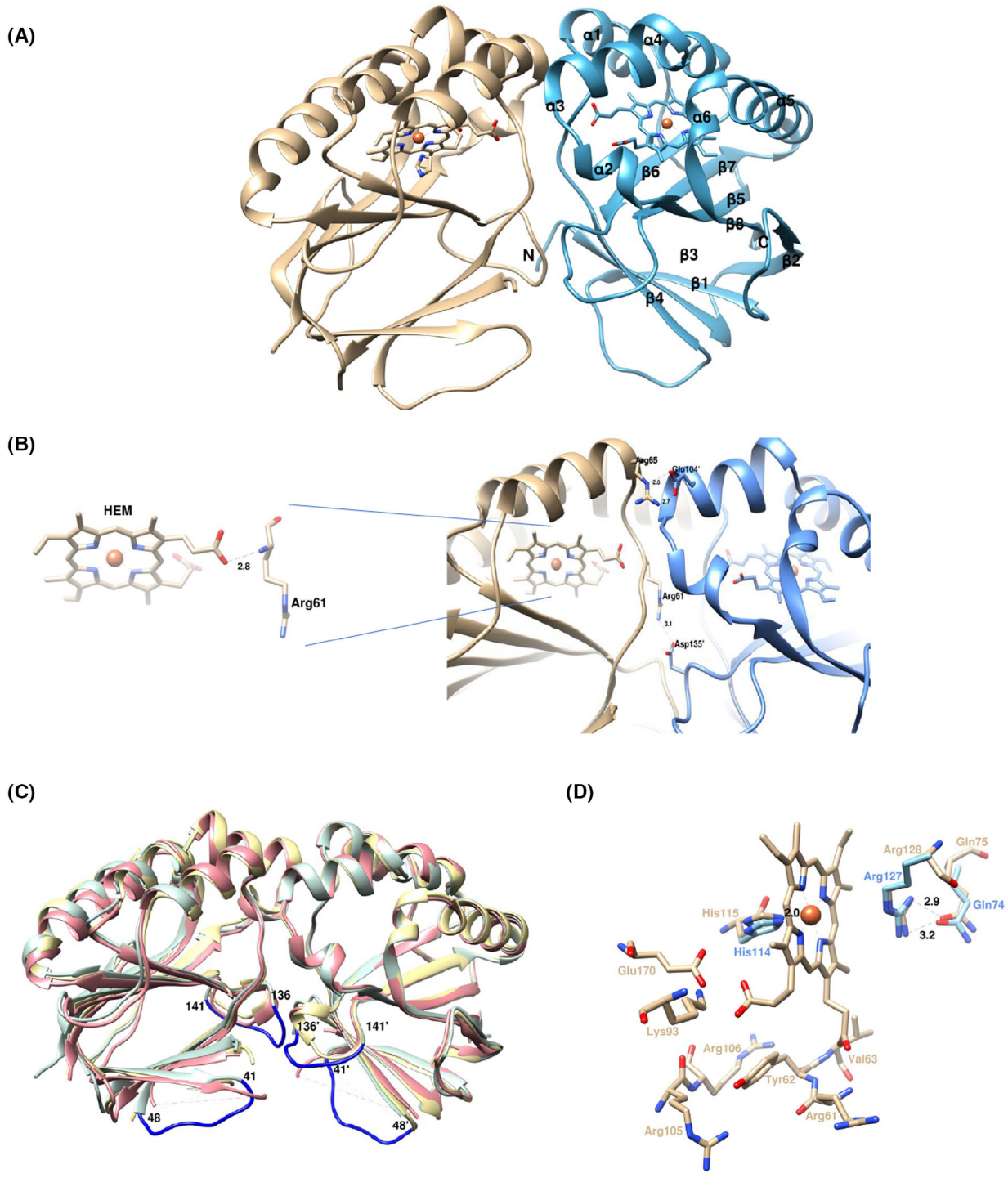

Fig. 8. *Pa*Cld structural details. (A) Ribbon representation of the dimeric structure of *Pa*Cld. Heme groups are depicted as gray sticks and iron as orange sphere. (B) Detailed view of the Arg65-Glu104′ and Arg61-Asp135′ pairs involved in salt bridges at the interface. (C) Superposition of *Pa*Cld (light green ribbon) with the dimeric Clds from *Cyanothece sp.* PCC7425 (PDB: 5K90) (yellow ribbon) and *Nitrobacter winogradskyi* (PDB: 3QPI) (pink ribbon) using the Needleman-Wunsch algorithm in BLOSUM-62. The overall RMSD was calculated equal to 0.613 Å and the Q-score was 0.852. Specifically, the RMSD of 5K90 chain A and *Pa*Cld chain A was calculated equal to 0.538. The RMSD between *Pa*Cld chain A with the 3QPI chain B was 0.686 Å. (D) Close-up view of the heme cavity. The flexible Arg128 and Arg127 of *Pa*Cld and CCld, respectively, are shown. The heme iron is depicted as orange sphere. Distances (in Å) between the heme iron His115 and Arg128-Gln75 are depicted as dashed lines. Figures were created with UCSF CHIMERA [34].

Leu123, Arg128, and Glu170 (numbering of *Pa*Cld) are also conserved in *Nw*Cld and *Cyanothece sp*. PCC7425, and in sequences that are closely related to these reference proteins [8,11]. The residues His115, Glu170, Lys93, Tyr62, Arg105, and Arg106 are conserved among functional chlorite dismutases; however, Arg105 is characteristic of clade 2 representatives [8]. These amino acids participate in different networks that stabilize heme and contribute to catalytic efficiency. A characteristic network of interactions involves His115, Glu170, Lys93, and heme substituent propionate 6 (Fig. 9A) [8,11,20]. This network shifts the reduction potential of the heme iron to more negative values [11]. At a distance of 3.93 Å from propionate group 6, there is a pair of tryptophan residues (Trp97 and Trp98) whose aromatic ring systems are oriented perpendicularly and form pi–pi interactions. Trp98 participates in a network with Lys93, Leu100, Arg105, and Ile108 for the stabilization and orientation of Trp97 for its interaction with the heme *b* propionate group. Trp97 also participates in the network of Lys93, Glu170, and His115. Therefore, both Trp residues appear to play a significant role in redox catalysis (Fig. 9A). Coulombic surface analysis showed a positive electrostatic potential on the surface around the entrance to the active sites (Fig. 9B). Cld structures exhibit the same characteristics in order to attract the anionic substrate chlorite [11]. Figure 9C shows the $2F_o - F_c$ electron density map of Arg128 contoured at 0.9σ.

Amino acid sequence analysis was conducted, incorporating Cld sequences from various species. The sequences were selected based on size (specifically shorter lineage 2a Clds) and included those from phyla abundant in Cld, such as Proteobacteria, Cyanobacteria, Nitrospirae, and Planctomycetes. The key residues essential for Cld activity, including the heme-binding arginine (R127), proximal heme lysine (K92), histidine (H114), and glutamic acid (E167), are conserved. In addition, Arg60, Tyr61 are conserved, while Val62 differs among species. However, the amino acids at positions 150 and 151 in the η3/α4 region of *Pa*Cld (S150, D151, E152, T153) differ from those in the corresponding positions of other Pseudomonas strains (E150, H151, T152, A153). These differences appear to alter the interaction network near the active site, potentially influencing enzyme activity or stability.

Conclusion

In this study, the dimeric structure of *Pa*Cld was resolved at 0.99 Å resolution, and the thermal inactivation kinetic(s) and the impact of chaotropic agents on the structural integrity of *Pa*Cld were reported. Amino acid networks that are considered significant for the catalytic activity of the enzyme and enzyme stability were identified. Beyond its role as a biomarker for chlorite, Cld participates in pathways involving reactive chlorine species, which remain to be fully elucidated. Additionally, Cld has significant applications, such as in water remediation. The thermostability and catalytic efficiency of the recombinant *Pa*Cld enzyme position it as a promising scaffold for engineering novel Cld enzymes with enhanced or unique catalytic properties.

Materials and methods

Materials

The designed primers used for the amplification of the full-length coding region of chlorite dismutase from *Pseudomonas sp*. (accession no. WP_026084028.1) were obtained from Macrogen-Europe. The amplicon was cloned into the expression vector pETite C-His (Lucigen Corporation, Middleton, WI, USA) for subsequent expression of a C-terminal His-tagged fusion enzyme. Kanamycin and sodium chlorite ($NaClO_2$) were purchased from AppliChem (Darmstadt, Germany) and Sigma-Aldrich, USA (Merck, Marousi, Greece), respectively. SYPRO™ Orange protein gel stain was purchased from Sigma-Aldrich (St. Louis, MO, USA). The In-Fusion®HD Cloning kit was obtained from Takara Bio USA, Inc., London, UK.

Methods

Gene isolation and molecular cloning

Gene-specific primers for *Pseudomonas aeruginosa* chlorite dismutase gene were designed according to the UniProt

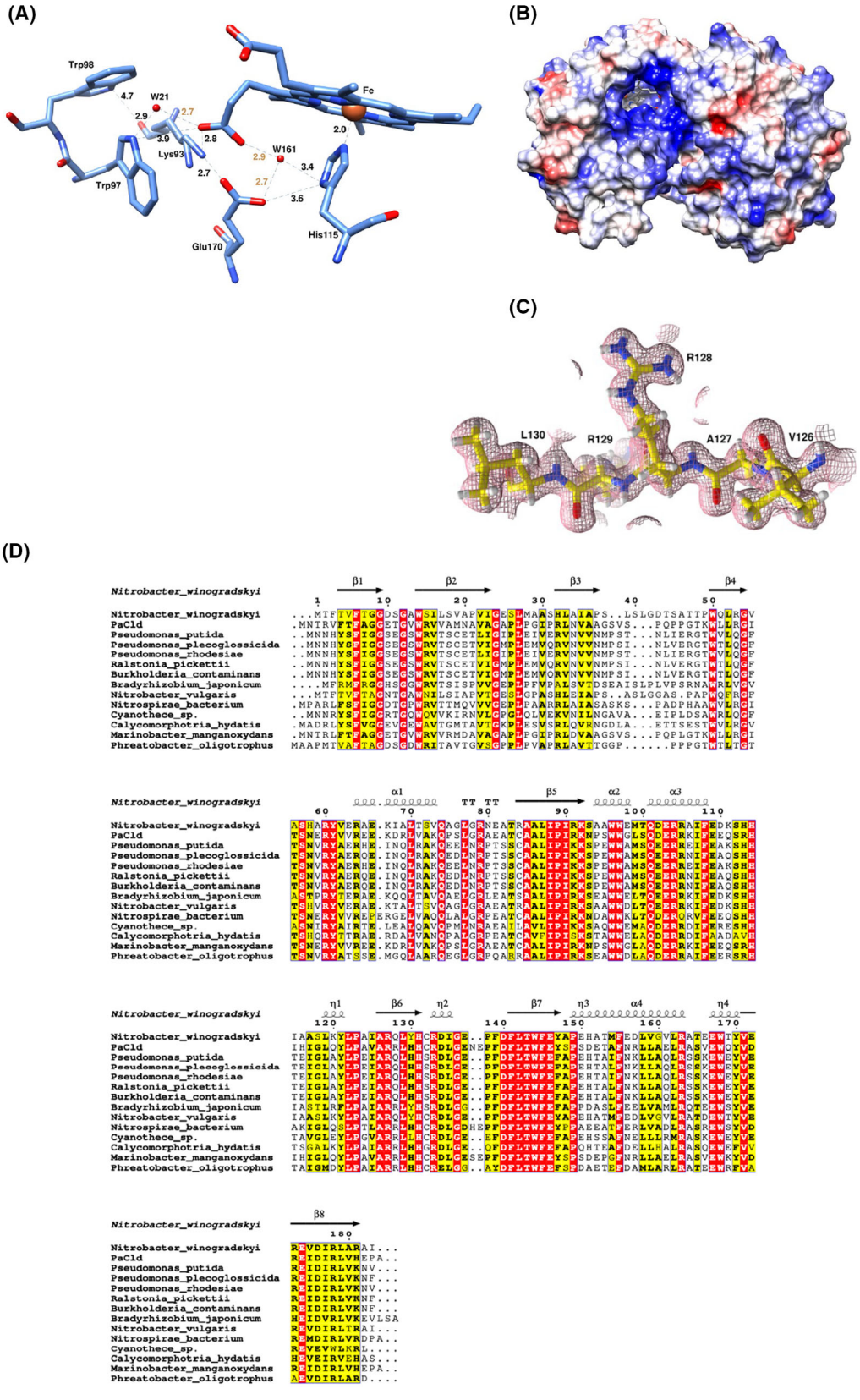

Fig. 9. Structure and sequence aspects of *Pa*Cld. (A) Interactions of heme propionate 6 with enzyme residues. Distances corresponding to H-bonds are colored in coral. Figure was created with UCSF CHIMERA [34]. (B) Coulombic surface representation of the *Pa*Cld holoenzyme. The Coulomb electrostatic surface shows regions of neutral (white), positive (blue), and negative (red) charge. Heme is presented as a stick model. The analysis was carried out using UCSF CHIMERA [34]. (C) $2F_o - F_c$ electron density of Arg128 contoured at 0.9σ. Figure was created with UCSF CHIMERA [34] (D) Amino acid sequence was conducted of different species based on size (shorter lineage 2a Cld) and phyla with a high percentage of Cld: Proteobacteria, Cyanobacteria, Nitrospirae, and Planctomycetes (*Nitrobacter winogradskyi* (strain ATCC 25391/DSM 10237/CIP 104748/NCIMB 11846/Nb-255) GenBank code: ABA05695.1; *Pseudomonas putida*, GenBank code: ACJ02339.1; *Pseudomonas plecoglossicida*, GenBank code: PBJ91937.1; *Pseudomonas rhodesiae*, GenBank code: SDV17268.1; *Ralstonia pickettii*, GenBank code: MRT01466.1; 6. *Burkholderia contaminans*, GenBank code: UXZ65922.1; 7. *Bradyrhizobium japonicum*, GenBank code: APG08518.1; *Nitrobacter vulgaris*, GenBank code: OPH82123.1; *Nitrospirae bacterium*, GenBank code: PJB95868.1; Cyanothece sp. (strain PCC 7425/ATCC 29141), GenBank code: ACL43807.1; *Calycomorphotria hydatis*, GenBank code: QDT67025.1; *Marinobacter manganoxydans*, GenBank code: EHJ03506.1; *Phreatobacter oligotrophus*, GenBank code: PTM55030.1).

database. The sequences of the primers were as follows: (forward) 5′-GAAGGA GAT ATA CAT ATG-AAT ACA CGA GTA TTT ACG TTC GC-3′ and (reverse) 5′-GTG ATG GTG GTG ATGATG-GGC CGG CTC ATG CAC TAG CCG-3′. The first 15 nucleotides of each primer correspond to regions of the expression vector pETite C-His Kan vector, and the rest of the sequence is gene-specific. Gene amplification was achieved through a gradient PCR protocol using KAPA Taq DNA polymerase and total genomic eDNA as a template that was extracted from a soil sample site collected aseptically from the surrounding area of the Children's Hospital 'Agia Sofia' in Athens, according to the instructions of the NucleoSpin® Soil kit (Macherey-Nagel, Germany). The quantity of the purified eDNA was determined using a NanoDrop®ND-1000 spectrophotometer (Thermo Fisher Scientific Inc., Waltham, MA, USA) and was found equal to 7.5 ng·μL^{-1}. Data analysis of 16S RNA sequencing was conducted using CD Genomics (NY, USA). The PCR mixture (total volume at 25 μL) consisted of the following components: 1.5 ng genomic DNA, from soil sample, 7.5 pmol of each primer, 50 μM of each dNTP, 10× KAPA Taq buffer, and 0.5 U KAPA Taq DNA polymerase. The selected PCR conditions were based on the manufacturer's instructions and included an initial denaturation at 95 °C for 3 min, three sets of 11 cycles with denaturation at 95 °C for 30 s, annealing temperatures at 52 °C, 54 °C, and 64 °C for 30 s, and extension at 72 °C for 60 s. A final extension at 72 °C for 10 min was performed. The PCR product was assessed by 1% w/v agarose gel electrophoresis, and the corresponding amplification fragment was cut off and purified using the NucleoSpin®Gel kit (Macherey-Nagel, Germany), according to the manufacturer's instructions. The purified DNA fragment was subsequently amplified by another PCR using the previous denaturation and extension conditions but one set of cycles with the annealing temperature at 64 °C. The components of the reaction were the same except for the template. In the second PCR, the gel-extracted purified DNA was used for gene amplification. The final product was evaluated via 1% w/v agarose gel electrophoresis and was inserted in the expressional pETite C-His vector following the instructions of In-Fusion®HD Cloning kit. The cloning reaction mixture was used to transform *E. coli* Stellar™ competent cells. Selected colonies were sequenced (Macrogen-Europe).

Heterologous expression and purification of PaCld

The recombinant expression of *Pa*Cld was tested in eight *E. coli* strains: Lemo21 (DE3), Rosetta (DE3), Rosetta (DE3) pLysS, pLysS, C41 (DE3), Tuner (DE3), BL21 (DE3), and Origami B (DE3). Finally, for the recombinant expression of *Pa*Cld, *E. coli* cells C41(DE3) were selected and grown in Luria-Bertani (LB) medium supplemented with kanamycin (30 μg·mL^{-1}). The culture was inoculated with a freshly prepared overnight culture (at a dilution ratio of 1 : 10) and was grown at 37 °C under agitation. When the optical density at 600 nm reached the value of 0.6 isopropyl-D-thiogalactopyranoside (IPTG) was added to a final concentration of 1 mM. After 4 h, cells were harvested by centrifugation (7500 ***g***; 10 min), resuspended in lysis buffer (50 mM NaH_2PO_4, 300 mM NaCl, 10 mM imidazole, pH 8), disrupted by sonication (50 W, 60 Hz, 5 cycles of 10 s sonication and 30 s interval, ice bath) and centrifuged twice at 16 000 ***g*** for 5 min. The enzyme purification was performed through metal affinity chromatography using Ni-IDA-Sepharose affinity absorbent and 50 mM NaH_2PO_4, 300 mM NaCl, pH 8 as equilibration buffer, while non-adsorbed protein was washed off with 10 mL wash buffer (50 mM NaH_2PO_4, 300 mM NaCl, pH 8). The enzyme was eluted using lysis buffer with a higher concentration of imidazole (250 and 350 mM). SDS/PAGE (12.5% w/v) was used for the evaluation of protein purity [35]. The purification yield of the enzyme was further assessed via analytical size-exclusion chromatography (SEC) using an analytical BioSep™ 5 μm SEC-S3000 290 Å column (size 300 × 7.8 mm) equilibrated with 100 mM phosphate buffer (pH 6.8). In addition, the Reinheitszahl value (Rz-value or purity number, $A_{Soret}412$ nm/A280nm) was estimated since it reflects the occupancy of the active site with the heme (prosthetic group) [20].

Chlorite degradation activity

Chlorite dismutase activity was measured using a Clark type oxygen electrode (HI9146 Portable Dissolved Oxygen Meter; Hanna Instruments Ltd, UK) following the release of O_2. Reactions were performed at 30 °C after calibration of the electrode with 100% O_2 air using an O_2-free phosphate buffer. The electrode was inserted in 100 mM phosphate reaction buffer, pH 6.0 (20 mL) at 30 °C with magnetic stirring (300 r.p.m.) to conduct a baseline and record non-enzymatic rates. Enzyme activity was measured by adding $NaClO_2$ at a final concentration of 1.9 mM. Dioxygen production rates (μM $O_2 \cdot s^{-1}$) were determined from the initial linear time values.

Enzymatic activity and the impact of pH

The pH profile and the determination of the optimal pH function were deduced by reactions carried out at 30 °C in 100 mM sodium acetate buffer (pH 4.0–6.0), 100 mM potassium phosphate buffer (pH 6.0–7.0) and 100 mM Trizma base buffer (pH 7.0–9.0). All measurements were corrected for non-enzymatic reactions using controls in the absence of the enzyme. The impact of pH on enzyme stability was studied by incubating the enzyme in buffers with different pH values for 120 min and then measuring enzyme activity. Typical measurements were performed in triplicate, with maximum deviations from the mean value of 10%. Curve-fits were obtained using GRAPHPAD (GraphPad Software Inc., version 7.00).

Steady-state kinetics and pH dependence of kinetic parameters

Steady-state kinetic analysis was carried out under the same conditions as the enzyme assay by adding different concentrations of $NaClO_2$ (0.01–3 mM) dissolved in 100 mM phosphate buffer (pH 7.0). The enzyme had been previously dialyzed against 20 mM phosphate buffer (20 mM NaH_2PO_4, pH 7). The same analysis was performed at different pH values (5.5, 6.0, and 6.5). Before the steady-state kinetic analysis, reaction rates were measured under different concentrations of the enzyme (0.007–0.07 μμ) in order to use the appropriate enzyme concentration that follows a linear relation with the reaction rate. Finally, a kinetic analysis was performed using 0.029 μμ of the enzyme. Molecular oxygen production rates were obtained from the initial linear time traces (35 s) and plotted against the sodium chlorite concentrations. Typical measurements for the steady-state kinetics plot were performed in triplicate, with a maximum deviation from the mean value of 10%. Curve-fits were obtained using the GRAPHPAD (GraphPad Software Inc., version 7.00) computer program. The irreversible inhibition mechanism of $HOCl^-$ from chlorite degradation was elucidated using methionine according to Hofbauer *et al.* [30].

Chemical denaturation followed by UV–vis spectroscopy

The chemical unfolding of the enzyme by guanidinium hydrochloride (GdnHCl) was monitored following the changes in the Soret peak by UV–vis spectrophotometry. A UV–vis spectrophotometer was used to scan the enzyme in different concentrations of GdnHCl at a scan speed of 120 nm·min^{-1}. For each GdnHCl concentration, the fraction α of the unfolded protein was calculated from the shift of the Soret maximum according to $\alpha = (A_N - A)/(A_N - A_U)$, where A represents the Soret band maximum at defined GdnHCl concentrations, A_N is the Soret maximum of the native state, and A_U is the Soret maximum of the completely unfolded state [3].

Thermal impact on enzyme activity

The thermal stability of *Pa*Cld was investigated using kinetics inactivation studies [36]. Thermal profiling was performed by determining residual enzymatic activities in the range of 10–75 °C (for 5 min incubation) using the optimum assay conditions at 30 °C for pH 6 and 7. Measurements of residual activity (enzyme activity at 10 °C was considered as 100%) were conducted to determine the temperature at which 50% of the initial enzyme activity is lost after heat treatment ($T_{1/2}$). The $T_{1/2}$ value was determined from the plot of relative inactivation (%) versus temperature (°C). In addition, the enzyme was exposed to high temperature of 67 °C, and the catalytic activity was recorded versus time. Graphs were obtained using the GRAPHPAD (GraphPad Software Inc., San Diego, CA, USA, version 7.00) computer program.

UV–vis spectra at different pH and temperature

UV−vis spectra of *Pa*Cld were recorded in a wavelength range from 320 to 700 nm for elucidation of changes in the Soret region attributed to temperature. The impact of the temperature on the Soret peak was evaluated by the spectral changes that were monitored between 320 and 700 nm by adding 11.3 μM of enzyme in phosphate buffer (20 mM KH_2PO_4, pH 7), which was incubated at a range of temperatures (10–90 °C) for 5 min, and the spectral changes were recorded. Enzyme UV–vis spectrum was also recorded under different pH values (with the appropriate buffer) at temperature 25 °C. Peaks were obtained using ORIGINLAB Software (OriginLab Corporation, Northampton, MA, USA).

Protein determination

Protein concentration was determined by the Bradford assay using BSA (fraction V) as a standard protein [37].

Crystallization

Prior to crystallization, the protein was concentrated to 13.7 mg·mL^{-1} in buffer Hepes 10 mM (pH 7.0), NaCl

100 mM, and NaN_3 0.002% w/v. Crystals were grown using the method of hanging drop vapor diffusion in Linbro plates. The drops consisted of 2.5 L of protein solution mixed with an equal volume of reservoir solution (PEG 3350 20% w/v, 0.2 M sodium citrate). The drops were equilibrated against 800 µL of reservoir solution at 16 °C. Crystals appeared after ~ 3 days.

Structure determination, refinement, and analysis

X-ray diffraction data were collected on the P13 beamline at PETRA III (DESY, Hamburg). *Pa*Cld crystals were found to belong to the C2 space group with unit cell dimensions $a = 127.5$ Å, $b = 46.0$ Å, $c = 90.2$ Å, and $\beta = 129.3°$, suggesting the presence of two molecules in the crystallographic asymmetric unit according to Matthews coefficient [38]. Initial phases were calculated with molecular replacement using PHASER [39] as implemented in PHENIX 1.20 [40]. A search model was constructed using SCULPTOR [41] and the crystal structure of a chlorite dismutase from *Cyanothece sp*. PCC7425 (PDB id: 5K90; sequence identity 54%) [8] as a template. Refinement was carried out with PHENIX 1.20, and the structure was visualized and rebuilt with COOT 0.8.9 [42]. The final structure was validated using MOLPROBITY [43] and tools available in COOT and PHENIX. Data collection and refinement statistics are shown in Table 4.

Acknowledgements

We thank Biocenter Finland and the Academy of Finland for infrastructure support and the staff at EMBL-Hamburg for their assistance during data collection. We also thank the Laboratory of Food Microbiology and Biotechnology of AUA for the Clark type O_2 electrode support, the Laboratory of Molecular Biology for the NanoDrop®ND-1000 spectrophotometer, and the staff of Children's Hospital 'Agia Sofia' in Athens for their assistance in soil sample collection.

Conflict of interest

The authors declare no conflict of interest.

Author contributions

DVN performed the experiments, analyzed data, and wrote the manuscript; EKP, AIK, and GEP performed the experiments and analyzed data; NEL analyzed data and wrote the manuscript; EKE performed experiments, analyzed data, and wrote the manuscript; ACP collected X-ray diffraction data, analyzed the X-ray structure, and wrote the manuscript; EGC planned experiments, performed and supervised experiments, analyzed data, and wrote the manuscript.

Data availability statement

All data are included in the article. The structural data are openly available in the Protein Data Bank (PDB: 9GTJ).

References

1 Zhang M, Xie X, Tang M, Criddle CS, Cui Y & Wang SX (2013) Magnetically ultraresponsive nanoscavengers for next-generation water purification systems. *Nat Commun* **4**, 1866.
2 Baresel C, Schaller V, Christian J, Johansson C, Bordes R, Chauhan V, Sugunan A, Sommertune J & Welling S (2019) Functionalized magnetic particles for water treatment. *Heliyon* **5**, e02325.
3 Hofbauer S, Gysel K, Mlynek G, Kostan J, Hagmüller A, Daims H, Furtmüller PG, Djinović-Carugo K & Obinger C (2012) Impact of subunit and oligomeric structure on the thermal and conformational stability of chlorite dismutases. *Biochim Biophys Acta* **1824**, 1031–1038.
4 EWG Tap Water Database. https://www.ewg.org/tapwater/contaminant.php?contamcode=1009.
5 Ueno H, Oishi K, Sayato Y & Nakamuro K (2000) Oxidative cell damage in Kat-sod assay of oxyhalides as inorganic disinfection by-products and their occurrence by ozonation. *Arch Environ Contam Toxicol* **38**, 1–6.
6 Celis AI, Geeraerts Z, Ngmenterebo D, Machovina MM, Kurker RC, Rajakumar K, Ivancich A, Rodgers KR, Lukat-Rodgers GS & DuBois JL (2015) A dimeric chlorite dismutase exhibits O2-generating activity and acts as a chlorite antioxidant in *Klebsiella pneumoniae* MGH 78578. *Biochemistry* **54**, 434–446.
7 European Food Safety Authority (EFSA) (2015) Risks for public health related to the presence of chlorate in food. *EFSA J* **13**, 4135.
8 Schaffner I, Mlynek G, Flego N, Pühringer D, Libiseller-Egger J, Coates L, Hofbauer S, Bellei M, Furtmüller PG, Battistuzzi G *et al.* (2017) Molecular mechanism of enzymatic chlorite detoxification: insights from structural and kinetic studies. *ACS Catal* **7**, 7962–7976.
9 Markhard AL, McCoy JG, To TL & Mootha VK (2022) A genetically encoded system for oxygen generation in living cells. *Proc Natl Acad Sci U S A* **119**, e2207955119.
10 Barnum TP & Coates JD (2023) Chlorine redox chemistry is widespread in microbiology. *ISME J* **17**, 70–83.
11 Mlynek G, Sjöblom B, Kostan J, Füreder S, Maixner F, Gysel K, Furtmüller PG, Obinger C, Wagner M,

Daims H *et al.* (2011) Unexpected diversity of chlorite dismutases: a catalytically efficient dimeric enzyme from *Nitrobacter winogradskyi*. *J Bacteriol* **193**, 2408–2417.
12 Dudley M, Salamone A & Nerenberg R (2008) Kinetics of a chlorate-accumulating, perchlorate-reducing bacterium. *Water Res* **42**, 2403–2410.
13 Jing-Xuan S & Shi-Lu C (2017) Significant electron transfer in heme catalysis: the case of chlorite dismutase. *J Catal* **348**, 40–46.
14 Spero MA, Jones J, Lomenick B, Chou TF & Newman DK (2022) Mechanisms of chlorate toxicity and resistance in *Pseudomonas aeruginosa*. *Mol Microbiol* **118**, 321–335.
15 Schaffner I, Hofbauer S, Krutzler M, Pirker KF, Bellei M, Stadlmayr G, Mlynek G, Djinovic-Carugo K, Battistuzzi G, Furtmüller PG *et al.* (2015) Dimeric chlorite dismutase from the nitrogen-fixing cyanobacterium Cyanothece sp. PCC7425. *Mol Microbiol* **96**, 1053–1068.
16 Kostan J, Sjöblom B, Maixner F, Mlynek G, Furtmüller PG, Obinger C, Wagner M, Daims H & Djinović-Carugo K (2010) Structural and functional characterisation of the chlorite dismutase from the nitrite-oxidizing bacterium "*Candidatus Nitrospira defluvii*": identification of a catalytically important amino acid residue. *J Struct Biol* **172**, 331–342.
17 Goblirsch B, Kurker RC, Streit BR, Wilmot CM & DuBois JL (2011) Chlorite dismutases, DyPs and EfeB: 3 microbial heme enzyme families comprise the CDE structural superfamily. *J Mol Biol* **408**, 379–398.
18 Serra I, Schmidt D, Pfanzagl V, Mlynek G, Hofbauer S, Djinović-Carugo K, Furtmüller PG, García-Rubio I, Van Doorslaer S & Obinger C (2022) Impact of the dynamics of the catalytic arginine on nitrite and chlorite binding by dimeric chlorite dismutase. *J Inorg Biochem* **227**, 111689.
19 Geeraerts Z, Heskin AK, DuBois J, Rodgers KR & Lukat-Rodgers GS (2020) Structure and reactivity of chlorite dismutase nitrosyls. *J Inorg Biochem* **211**, 111203.
20 Hofbauer S, Gysel K, Bellei M, Hagmüller A, Schaffner I, Mlynek G, Kostan J, Pirker KF, Daims H, Furtmüller PG *et al.* (2014) Manipulating conserved heme cavity residues of chlorite dismutase: effect on structure, redox chemistry, and reactivity. *Biochemistry* **53**, 77–89.
21 Harrison BS, Eberli D, Lee SJ, Atala A & Yoo JJ (2007) Oxygen producing biomaterials for tissue regeneration. *Biomaterials* **28**, 4628–4634.
22 Gnanaprakasam ET, Lloyd JR, Boothman C, Ahmed KM, Choudhury I, Bostick BC, van Geen A & Mailloux BJ (2017) Microbial community structure and arsenic biogeochemistry in two arsenic-impacted aquifers in Bangladesh. *MBio* **8**, e01326-17.
23 Thakur M, Medintz IL & Walper SA (2019) Enzymatic bioremediation of organophosphate compounds—Progress and remaining challenges. *Front Bioeng Biotechnol* **7**, 289.
24 Blanc B, Rodgers KR, Lukat-Rodgers GS & DuBois JL (2013) Understanding the roles of strictly conserved tryptophan residues in O_2 producing chlorite dismutases. *Dalton Trans* **42**, 3156–3169.
25 Feng H, Liao X, Yang R, Chen S, Zhang Z, Tong J, Liu J & Wang X (2023) Generation, toxicity, and reduction of chlorinated byproducts: overcome bottlenecks of electrochemical advanced oxidation technology to treat high chloride wastewater. *Water Res* **230**, 119531.
26 Hu B, Yu H, Zhou J, Li J, Chen J, Du G, Lee SY & Zhao X (2023) Whole-cell P450 biocatalysis using engineered Escherichia coli with fine-tuned Heme biosynthesis. *Adv Sci (Weinh)* **10**, e2205580.
27 Hofbauer S, Schaffner I, Furtmüller PG & Obinger C (2014) Chlorite dismutases – a heme enzyme family for use in bioremediation and generation of molecular oxygen. *Biotechnol J* **9**, 461–473.
28 Hofbauer S, Bellei M, Sündermann A, Pirker KF, Hagmüller A, Mlynek G, Kostan J, Daims H, Furtmüller PG, Djinović-Carugo K *et al.* (2012) Redox thermodynamics of high-spin and low-spin forms of chlorite dismutases with diverse subunit and oligomeric structures. *Biochemistry* **51**, 9501–9512.
29 Streit BR, Blanc B, Lukat-Rodgers GS, Rodgers KR & DuBois JL (2010) How active-site protonation state influences the reactivity and ligation of the heme in chlorite dismutase. *J Am Chem Soc* **132**, 5711–5724.
30 Hofbauer S, Gruber C, Pirker KF, Sündermann A, Schaffner I, Jakopitsch C, Oostenbrink C, Furtmüller PG & Obinger C (2014) Transiently produced hypochlorite is responsible for the irreversible inhibition of chlorite dismutase. *Biochemistry* **53**, 3145–3157.
31 Jakopitsch C, Pirker KF, Flemmig J, Hofbauer S, Schlorke D, Furtmüller PG, Arnhold J & Obinger C (2014) Mechanism of reaction of chlorite with mammalian heme peroxidases. *J Inorg Biochem* **135**, 10–19.
32 Blanc B, Mayfield JA, McDonald CA, Lukat-Rodgers GS, Rodgers KR & DuBois JL (2012) Understanding how the distal environment directs reactivity in chlorite dismutase: spectroscopy and reactivity of Arg183 mutants. *Biochemistry* **51**, 1895–1910.
33 Schmidt D, Serra I, Mlynek G, Pfanzagl V, Hofbauer S, Furtmüller PG, Djinović-Carugo K, Van Doorslaer S & Obinger C (2021) Arresting the catalytic arginine in chlorite Dismutases: impact on Heme coordination, thermal stability, and catalysis. *Biochemistry* **60**, 621–634.
34 Pettersen EF, Goddard TD, Huang CC, Couch GS, Greenblatt DM, Meng EC & Ferrin TE (2004) UCSF chimera-a visualization system for exploratory research and analysis. *J Comput Chem* **25**, 1605–1612.

35 Laemmli UK (1970) Cleavage of structural proteins during the assembly of the head of bacteriophage T4. *Nature* **227**, 680–685.
36 Chronopoulou EG, Mutabdzija L, Poudel N, Papageorgiou AC & Labrou NE (2023) A key role in catalysis and enzyme Thermostability of a conserved helix H5 motif of human glutathione transferase A1-1. *Int J Mol Sci* **24**, 3700.
37 Bradford M (1976) A rapid and sensitive method for the quantitation of microgram quantities of protein utilizing the principle of protein-dye binding. *Anal Biochem* **72**, 248–254.
38 Matthews BW (1968) Solvent content of protein crystals. *J Mol Biol* **33**, 491–497.
39 McCoy AJ, Grosse-Kunstleve RW, Adams PD, Winn MD, Storoni LC & Read RJ (2007) Phaser crystallographic software. *J Appl Cryst* **40**, 658–674.
40 Liebschner D, Afonine PV, Baker ML, Bunkóczi G, Chen VB, Croll TI, Hintze B, Hung LW, Jain S, McCoy AJ *et al.* (2019) Macromolecular structure determination using x-rays, neutrons and electrons: recent developments in phenix. *Acta Crystallogr D* **75**, 861–877.
41 Bunkoczi G & Read RJ (2011) Improvement of molecular-replacement models with Sculptor. *Acta Crystallogr D* **67**, 303–312.
42 Emsley P & Cowtan K (2004) Coot: model-building tools for molecular graphics. *Acta Crystallogr D* **60**, 2126–2132.
43 Williams CJ, Headd JJ, Moriarty NW, Prisant MG, Videau LL, Deis LN, Verma V, Keedy DA, Hintze BJ, Chen VB *et al.* (2018) MolProbity: more and better reference data for improved all-atom structure validation. *Protein Sci* **27**, 293–315.